

SUB-10 CM SPACE DEBRIS: DETECTION AND INITIAL ORBIT DETERMINATION WITH A STAR TRACKER

Joel Filho^(1,2,3), Paulo Gordo^(2,3), Nuno Peixinho⁽¹⁾, Rui Melicio^(3,4,5), Paulo Garcia^(6,7)

⁽¹⁾ Instituto de Astrofísica e Ciências do Espaço, Universidade de Coimbra, Portugal

⁽²⁾ LIP, Faculdade de Ciências da Universidade de Lisboa, Portugal

⁽³⁾ Synopsis Planet, Advance Engineering Unipessoal LDA, 2810-174 Almada, Portugal

⁽⁴⁾ IDMEC, Instituto Superior Técnico, Universidade de Lisboa, Portugal,

⁽⁵⁾ AEROG, Universidade da Beira Interior, Covilhã, Portugal

⁽⁶⁾ Faculdade de Engenharia da Universidade do Porto, Portugal

⁽⁷⁾ INESC TEC, 4200-465 Porto, Portugal

Email: jafilho@fc.ul.pt; paulo.gordo@synopsisplanet.com; peixinho@uc.pt; ruimelicio@gmail.com; pgarcia@fe.up.pt

ABSTRACT

With space activities rapidly growing, cataloguing undetected debris ≤ 10 cm is critical for mission safety. This study uses ESA's GODOT software to simulate a small star tracker in orbit, detecting debris ≤ 10 cm and determining their initial orbits. The star tracker was simulated using GODOT's Python packages to observe debris over one day, considering sensor limitations like brightness and range distance. Results demonstrated that the star tracker can detect debris ≤ 10 cm during specific intervals. These detections were converted into angular measurements for input into angles-only initial orbit determination (IOD) methods, like Gauss and Gooding. Comparisons with simulation data show that IOD methods provided satisfactory results for the semimajor axis, position and velocity. Also, the inclination is estimated with reasonable accuracy for high-inclination orbits. This work highlights GODOT's versatility and demonstrates that a small star tracker can detect debris and provide initial orbit information on objects ≤ 10 cm.

1 INTRODUCTION

The Space Surveillance Network (SSN), a set of optical and radar telescopes, observes and maintains a catalogue of space objects in Earth's orbit larger than 10 cm. This catalogue is vital for space missions since it is used to perform avoidance manoeuvres. However, objects of this size represent only a tiny amount of the total, and the problem is even greater, whereas a collision with space debris ranging from 1 cm to 10 cm can be a catastrophic event [1–4]. In this context, alternative solutions to detect uncatalogued debris play a vital role in the future of space missions.

In this context, this work proposes using a small commercial star tracker that will soon fly to detect uncatalogued debris. Applying small space cameras like star trackers to observe space objects is not a new topic in literature. The studies of [5, 6] propose a similar approach to this paper. Both works developed an

analysis of using a star tracker to detect space debris, starting from the definition of the target orbit, then the computation of the sensor sensitivity, and finishing with detection simulations. However, the scope of these references is distinct from this paper since the first work concentrates on studying the most promising orbit position for a space-based mission to detect space debris, and the second focuses on the detection algorithm used.

Other studies can also be highlighted by their contributions to studying the sensitivity and performance of a sensor detecting space debris and simulating the detection in orbit [7–14]. Despite some works already published on this topic, this proposed paper contributes to demonstrating the entire mission analysis of using a commercial star tracker for detecting uncatalogued debris. This analysis starts by selecting the most likely orbit to detect space objects of the population of interest, considering the sensor limitations and space-based optical observation constraints. Another contribution is applying GODOT for the detection simulation and IOD, showing how powerful and versatile this ESA software is. IOD consists of the determination of the orbit of an object without previous information. The orbit computed by IOD methods usually has low accuracy, but it can provide some parameters, like the semimajor axis and inclination, with a high level of fidelity [15–17].

Several IOD methods exist depending on the type of data. As this work focuses on optical observations, only the classical angles-only IOD techniques will be considered, such as the Gauss and Gooding methods [18, 19].

2 POPULATION OF INTEREST

The commercial star tracker considered in this study is being developed by Synopsis Planet, which will fly onboard the New Space Portuguese Constellation. As this constellation will be placed in a Sun Synchronous orbit (SSO) of 550 km altitude, only uncatalogued

objects in the Low Earth Orbit (LEO) will be considered in the study. To evaluate the most probable region to find debris ranging from 1 cm to 10 cm, the ESA MASTER (Meteoroid and Space Debris Terrestrial Environment Reference) model was used. MASTER is a tool that provides the flux and spatial density of Earth's orbital environment.

Therefore, the spatial distribution of space debris ranging from 1 cm to 10 cm in LEO is shown in Fig. 1. The highest concentration of objects starts to increase around 600 km and reaches its maximum of around 800 km altitude. There is also a smaller concentration peak, around 1500 km. Since the target objects are tiny debris, the chances of the star tracker detecting them will be larger if they are close to the constellation. In other words, the ideal region is around the first concentration peak, at altitudes from 630 km to 880 km.

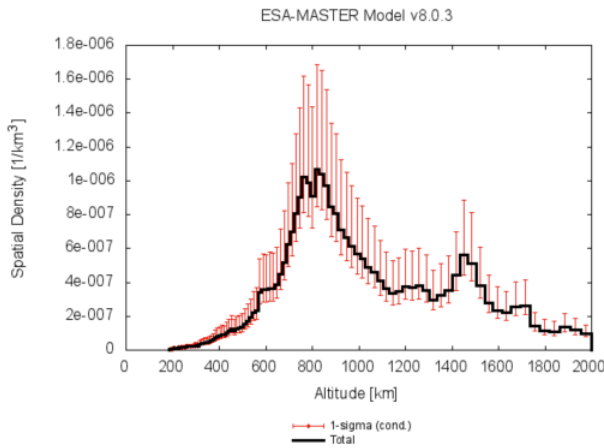


Figure 1. Space debris ranging from 1 cm to 10 cm spatial distribution in LEO [20].

MASTER also provides the orbits of these objects. So, the debris in the higher spatial density concentrates in approximately circular orbits with a semimajor axis ranging from 6550 km to 8950 km, inclinations from 40° to 120°, and right ascension of ascending node (RAAN) ranging in the entire interval, from -180° to 180°.

3 OPTICAL DETECTION PERFORMANCE

The detection performance of an optical sensor can be evaluated using the signal-to-noise ratio (SNR). In other words, if the signal emitted by the space debris is above the minimum threshold signal that the sensor can detect. This performance will be analysed by calculating the ratio of object signal per noise. This computation was done following PROOF (Program for Radar and Optical Observation Forecasting), an ESA software used to assess the performance of optical sensors in detecting space objects [21].

3.1 Signal-to-noise ratio analyses

The SNR refers to a ratio between the object signal and all the possible noise sources, such as the sensor's intrinsic noise and background noise. The signal of a space debris indicates how much light is reflected by the object [22] and it can be calculated by determining its irradiance [23]:

$$H = \frac{H_{sol} A \rho}{R^2} \frac{2}{3\pi^2} (\sin \phi + (\pi - \phi) \cos \phi) \quad (1)$$

In Eq. 1, H represents the irradiance of a spherical object, which is a reasonable approximation for space debris. Moreover, A , ρ and R are the object cross-section area, albedo and distance observer-object, also known as the range, respectively. Eq. 1 also accounts for the irradiance of the Sun and the solar phase angle ϕ . With the irradiance, one can compute the signal of the debris for a space-based scenario as:

$$S_{debris} = \frac{\pi}{4} D^2 t \int_{\lambda_0}^{\lambda_f} \frac{H q_{\lambda} \lambda}{hc} d\lambda \quad (2)$$

The signal is a sum over the desired wavelength λ interval of the irradiance and quantum efficiency q divided by the photon energy (hc/λ), with h being the Planck constant and c being the light speed. Eq. 2 also considers the aperture of the optical system D and the integration time t .

Besides that, the debris is a moving object, meaning its signal will spread over multiple pixels. Therefore, the signal of a moving object has to take into account also the number of pixels filled during an integration time, which is calculated by:

$$n_{pix} = \frac{\sqrt{n_{pix0}} v_{rel} t}{PS} \quad (3)$$

The number of pixels of a moving source depends on the minimal number of pixels (sensor Point Spread Function) a point-like source occupies in the sensor (n_{pix0}), the object's relative angular velocity (v_{rel}), the sensor's pixel scale (PS) and the integration time.

Until now, only the signal part of the SNR was considered. Moving to the noise computation, there are several types of noise, but only the continuous sources of background noise and the sensor noise were evaluated. The continuous source of background noise is related to the signal emitted by the galaxies and the Zodiacal light. This can be calculated using Eq. 2, considering the irradiance of these sources.

For the galaxies, the signal was computed using the zero-magnitude star spectral distributions for different wavelengths, presented in Tab. 1, assuming it has a uniform distribution in space. For Zodiacal light, the signal slightly varies for different wavelengths. So, the maximum value of $10^4 e^-/\text{pixel}/s$ was considered as the emitted signal [21].

Table 1. Spectral distribution over different wavelengths for zero-magnitude stars. Table extracted from PROOF

Wavelength [μm]	Spectrum quantities [$\frac{\text{W}}{\text{cm}^2\mu\text{m}}$]
0.0	0.0
0.1	0.25e-12
0.2	8.0e-12
0.3	9.5e-12
0.4	7.0e-12
0.5	4.75e-12
0.6	3.0e-12
0.7	2.0e-12
0.8	1.5e-12
0.9	1.0e-12
1.0	0.75e-12

After calculating the galaxies' signal using Eq. 2 and Tab. 1, the determined value is added to the Zodiacal light signal to find the background noise. Finally, with all the variables considered, the SNR can be computed as:

$$SNR = \frac{S_{debris}}{\sqrt{\sum noise}} \quad (4)$$

being,

$$\sum noise = n_{pix}S_r + S_{debris} + n_{pix}(S_B + S_d t) + \sqrt{n_{pix}v_{rel}S_r t} + \sqrt{n_{pix}v_{rel}t(S_B + S_d t)} \quad (5)$$

where S_r is the readout noise, S_d is the dark noise and S_B is the background noise.

3.2 Star tracker properties

Synopsis Planet's star tracker is a dual-purpose device: a star tracker and a space debris detection camera. This equipment was developed in the New Space framework using Commercial Off-The-Shelf (COTS) components and designed for CubeSats and small satellites. A 3D model of the star tracker is shown in Fig. 2, and its properties are presented in Tab. 2.



Figure 2. Synopsis Planet's star tracker 3D model.

The star tracker's image sensor is the commercial sensor AR0134 from Onsemi, and its datasheet provides the sensor's quantum efficiency, which is required in Eq. 2.

Table 2. Star tracker properties

Parameter	Typical Value
Active Pixels	1280 × 960 px CMOS
Pixel size	3.75 μm
Dynamic Range	64 dB
Readout noise	11.96 e^-
Dark noise	0.12 $e^-/\text{pixel}/\text{s}$
Aperture	9.5 mm
Focal length	16 mm
f-number	1.68
Full field of view (FOV)	21° (diagonal)
Dimensions (W × L × H) without baffle	47.1 × 42.1 × 28.5 mm
Mass (no baffle)	97.7 g
Point Spread Function (PSF)	9 pixels
Exposure time	0.2 s

3.3 Results

Considering Eqs. 1-5 and the parameters from Tab. 1 and Tab. 2, the performance of the star tracker in detecting space debris can be computed and analysed. To do so, five different sizes of objects varying from 1 cm to 10 cm were considered, and SNR was calculated by increasing the range of each object.

Since the phase angle and albedo are challenging to estimate, the analyses focused on these two parameters. First, the SNR was computed for different values of phase angles, fixing the albedo. Then, the calculation was performed by varying the albedo for a fixed phase angle.

Therefore, considering the average space debris albedo of 0.175, Fig. 3 shows the star tracker performance for three different values of phase angle. The dashed line represents the camera's minimal SNR or the camera's limit for seeing something.

Fig. 3 demonstrates the influence of the phase angle on the results. At a lower value, the star tracker can detect 3 cm objects up to 60 km and 10 cm debris up to a maximum range of 180 km. The performance decreases by increasing the phase angle. For an angle of 100°, for example, the camera can only detect objects larger than 6 cm for smaller ranges. The last scenario, an angle of 130°, represents the maximum possible value to detect an uncatalogued object by the proposed star tracker. However, the scenarios of lower phase angles will be more realistic since the camera is being developed to work with a large Sun exclusion angle.

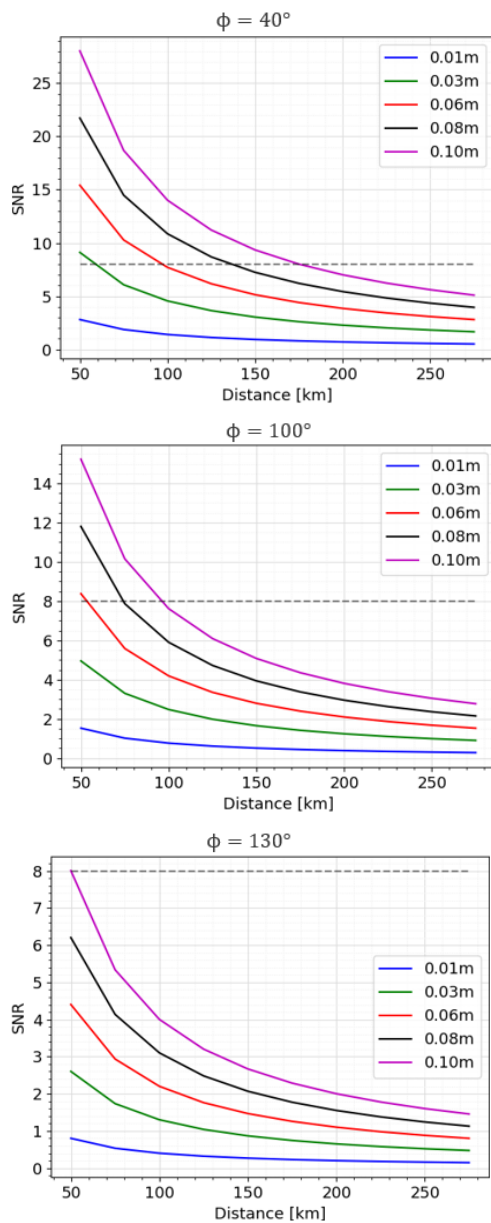


Figure 3. SNR over distance for five distinct object sizes in three scenarios of phase angle.

Moving to the albedo analyses. This property is material-dependent, i.e. different materials have distinct albedos. In addition, it isn't easy to find albedo estimates in the literature. So, the analysis was done by using the proposed estimates in PROOF in which fragments are considered to have an albedo of 0.2, Multi-Layer Insulation (MLI) materials of 0.56, and Sodium-potassium alloy (NaK) droplets of 0.85 for a fixed phase angle of 40°. Fig. 4 shows the performance of the star tracker for these three values.

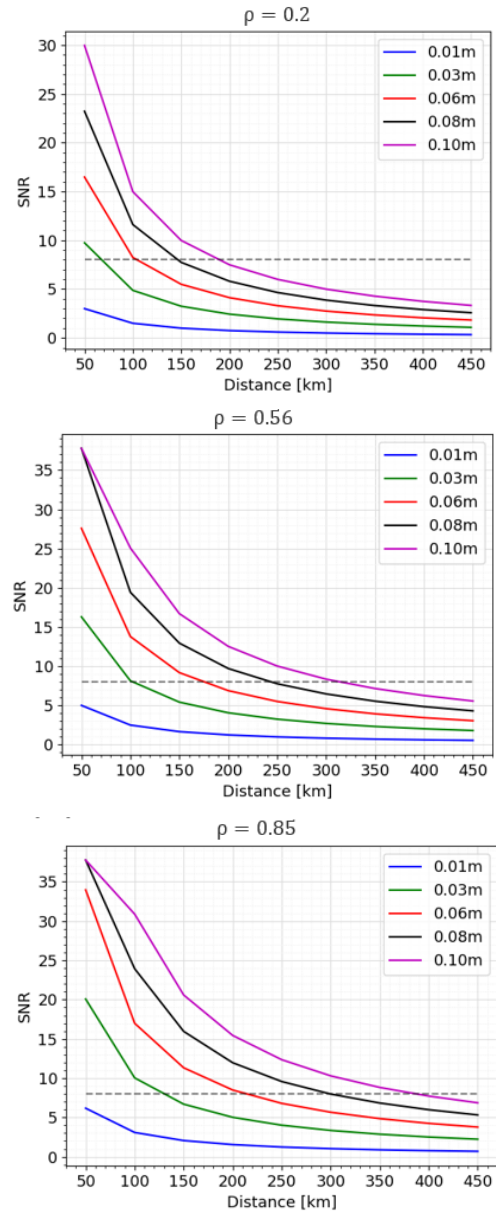


Figure 4. SNR over distance for five distinct object sizes with different materials.

Fig. 4 shows the impact of the material properties on the

performance of the star tracker. The higher the albedo, the farther an object can be detected. So, depending on the material, the camera will be able to detect uncatagued debris for a maximum distance ranging from 200 km to 400 km.

4 SIMULATIONS

The simulations consist of simulating the star tracker in a specific orbit, considering the sensor limitations, and trying to detect uncatagued debris from the most common region to find these objects. Furthermore, a space-based detector simulation has to take into account the following conditions [23]:

- The object must be outside the Earth's shadow to be illuminated by the Sun. In other words, the angular distance debris-shadow (ζ) has to be $\zeta > 0^\circ$.
- The phase angle ϕ ranges from zero degrees to a maximum value depending on the camera constraints.
- To guarantee that the Earth is outside the camera's FOV, the angular distance camera-Earth γ has to respect Eq. 6, in which the parameter ξ indicates a safety margin (a 5° distance is sufficient):

$$\gamma > \sin^{-1}\left(\frac{R_{Earth}}{\|\mathbf{x}_{obs}\|}\right) + \xi \quad (6)$$

- The object range must be inside the maximum distance the camera can detect.
- The object has to be inside the camera's FOV.

Fig. 5 shows the visualisation of the conditions. Moreover, using trigonometry, the required angular distances ϕ , ζ and γ can be calculated as [23]:

$$\phi = \cos^{-1}\left(\frac{(\mathbf{x}_{debris} - \mathbf{x}_{obs}) \cdot (\mathbf{x}_{debris} - \mathbf{x}_{Sun})}{\|\mathbf{x}_{debris} - \mathbf{x}_{obs}\| \|\mathbf{x}_{debris} - \mathbf{x}_{Sun}\|}\right) \quad (7)$$

$$\zeta = \pi - \cos^{-1}\left(\frac{\mathbf{x}_{Sun} \cdot \mathbf{x}_{debris}}{\|\mathbf{x}_{Sun}\| \|\mathbf{x}_{debris}\|}\right) - \sin^{-1}\left(\frac{R_{Earth}}{\|\mathbf{x}_{debris}\|}\right) \quad (8)$$

$$\gamma = \cos^{-1}\left(\frac{\mathbf{x}_{obs} \cdot (\mathbf{x}_{obs} - \mathbf{x}_{debris})}{\|\mathbf{x}_{obs}\| \|\mathbf{x}_{obs} - \mathbf{x}_{debris}\|}\right) \quad (9)$$

Using Eqs. 7-9, the angular distances can be easily computed if the positions of the observer, debris and Sun relative to the Earth's centre are known.

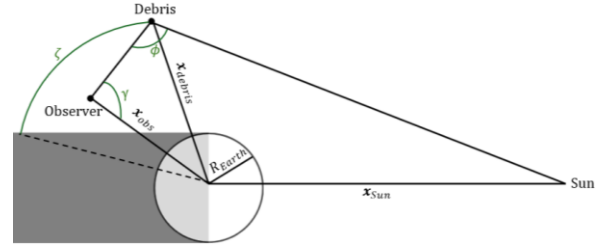


Figure 5. Space-based illustrated conditions. Image adapted from [17].

4.1 Simulator

The simulator was constructed using the ESA standard software for flight dynamics analysis, GODOT [24]. This software was developed at ESA/ESOC (European Space Operations Centre) to estimate, optimise and analyse space missions.

Using the GODOT environment, one can define the physics in orbit, create objects to be propagated and perform the desired analyses. In this sense, the simulator was developed based on the physics for Earth-orbiting objects, with the Earth's centre as a frame system and considering the dynamics and perturbations of LEO. Then, the space-based was defined in the SSO of 550 km. Tab. 3 presents its initial state.

Table 3. Space-based initial state

a	e	i	RAAN	Epoch
6924 km	0.0001	97.6°	299.86°	2024-04-22T04:04:44.180 UTC

After that, the objects to be detected were simulated considering the MASTER output, presented in Section 2, of the most probable region to find uncatagued debris. The orbits of these objects have six different values of semimajor axis apart from 50 km, ranging from 7000 km to 7250 km. Each semimajor axis has ten different values equally spaced in inclination and RAAN ranging from 40° to 120° and -180° to 180° , respectively. Moreover, the orbits are approximately circular with an eccentricity of 0.001. Therefore, 600 distinct orbit scenarios were simulated for one-day propagation starting at the epoch of the space-based.

The conditions for object detection by the space-based were classified as events. In this way, every time the conditions were reached, GODOT output the times when this happened. Five events were created to consider the five conditions.

The first event analyses if the object is outside the Earth's shadow $\zeta > 0^\circ$. The second one calculates if the phase angle ϕ is inside the defined interval. In this case, an interval ranging from 0° to 40° . The third event

computes the angular distance camera-Earth γ to verify if Eq. 6 stands. The fourth determines the distance between the space-based and debris. This event is considered if this distance is smaller than the maximum range the camera can detect an object. Finally, the last event checks if the debris is inside the FOV by converting the object's vectorial distance into spherical coordinates.

The simulations were performed three times with different maximum ranges reached by the camera to consider objects of distinct materials. As seen in Section 3, if the debris is a fragment object, the maximum camera range is 200 km. If it has an MLI material, this value increases to 300 km, and it is even higher, reaching 400 km, if the debris is NaK droplets.

4.2 Results

The objective of the simulation is to assess if the star tracker can detect some objects in the 600 different orbits. The simulation was performed as follows: for each semimajor axis, a hundred orbits varying the inclination and RAAN were propagated. The 600 distinct simulated orbits are reached due to the use of six values of the semimajor axis.

These 600 simulated orbits were run three times by changing the maximum range at which the camera could detect an uncatalogued object to evaluate the influence of different materials on the star tracker's performance. Fig. 6 shows the number of objects the camera detects for the different semimajor axis orbits considering the three scenarios for the maximum range.

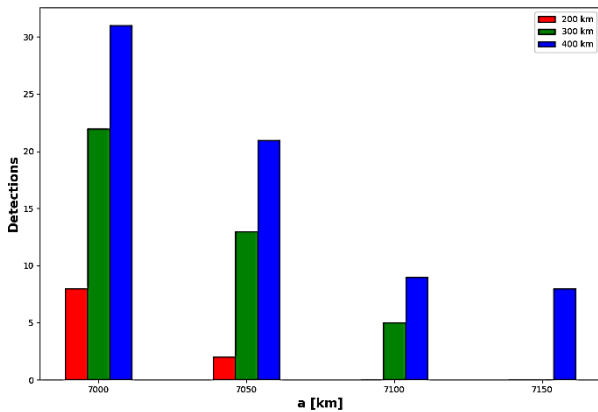


Figure 6. Star tracker detection for the several simulated scenarios.

The results demonstrate that the star tracker can detect some debris in one day of observation since each bar represents the number of occurred detections. The influence of the material in the detections can also be noticed, as larger albedo objects have more chances to be observed. The camera can detect faint debris until 7050 km of semimajor axis orbits, reaching brighter

objects in more distant orbits with the semimajor axis of 7150 km.

However, the star tracker could not detect objects beyond the orbits with a semimajor axis of 7150 km. So, from the six semimajor axis orbits, the observation occurred only for the first four semimajor axis.

Therefore, the simulations confirm that the star tracker in an SSO orbit looking at the uncatalogued debris in the most crowded region can detect a satisfactory number of objects for several orbit scenarios, with the debris in closer orbits more probable to be observed.

5 INITIAL ORBIT DETERMINATION

Angles-only initial orbit determination methods are techniques developed to determine an object's orbit using angular data provided by optical observations, such as the right ascension (RA), declination (DEC), and observation time. The methods consist of using this known information to determine the position vector of the observed object. Since the position vector requires six independent quantities to be entirely determined, at least three sets of observation data are needed.

The position vector of an Earth-orbiting object observed by an optical sensor can be calculated as [18]:

$$\vec{r} = \rho \hat{L} + \vec{r}_{site} \quad (10)$$

Where ρ is the distance observer-object, the range, \vec{r}_{site} is the observation site (the space-based location in this context), and \hat{L} is the line-of-sight unit vector. This vector can be computed using the RA and DEC as:

$$\hat{L} = \begin{bmatrix} \cos(DEC) \cos(RA) \\ \cos(DEC) \sin(RA) \\ \sin(DEC) \end{bmatrix} \quad (11)$$

Therefore, the Angles-only IOD methods implement different techniques to find the range and, consequently, determine the object position vector.

5.1 Simulated results into angular data

The output of the simulation is the interval of time an object in a specific region will be visible to the star tracker and the orbit of this object. In other words, if the camera takes pictures during this time interval, it will detect this debris. For example, an object in an orbit of 7100 km of semimajor axis, 84.44° of inclination and 138.06° of RAAN will be visible for time intervals starting at 07:43:46 UTC until 07:44:11 UTC on the same day, 2024-04-22. So, the debris is visible for about 25 seconds.

However, the output data must be converted into angular data, RA and DEC to apply the simulation results in the angles-only IOD methods. In this sense, considering that the star tracker takes pictures every 5 seconds (since the star tracking needs at least 3 seconds

to process the image), the detection will be separated by 5 seconds during the visible time. For instance, using the visible time interval presented in the last paragraph, five detections of the same object, or at least four if accounting for the integration time, will occur. Therefore, only the results of visible time intervals greater than 20 seconds were chosen to ensure at least three observations of the same debris.

After that, the GODOT was used to propagate the orbit of the chosen object to the observation times since the output orbit from the simulation has the starting time of the visible time interval as its initial state. The propagation is required to know the exact debris position vector at that specific time. With the position vector and the observation site, the slant range vector $\vec{\rho} = \rho \hat{L}$ can be computed by using Eq. 10. Thereafter, the RA and DEC can be calculated as:

$$DEC = \sin^{-1} \left(\frac{\vec{\rho} \cdot \hat{K}}{\|\vec{\rho}\|} \right) \quad (12)$$

$$\text{if } \frac{\vec{\rho} \cdot \hat{J}}{\|\vec{\rho}\|} > 0, RA = \cos^{-1} \left(\frac{(\vec{\rho} \cdot \hat{I}) / \|\vec{\rho}\|}{\cos DEC} \right) \quad (13)$$

$$\text{else, } RA = 360^\circ - \cos^{-1} \left(\frac{(\vec{\rho} \cdot \hat{I}) / \|\vec{\rho}\|}{\cos DEC} \right) \quad (14)$$

Then, these values of RA, DEC, and observation times represent the angular data of an object provided by optical observation. Moreover, to increase the fidelity of the calculated data, since the camera is not a perfect device, the values of RA and DEC were corrupted with an error of 3 arcsec. This is the predicted uncertainty of the star tracker's attitude results.

Therefore, a Monte Carlo simulation was performed to take a hundred random values corrupted by the three arcsec uncertainty for the RA and DEC of each observation time. In other words, every observation time will have a hundred random values of RA and DEC corrupted by the star tracker's error.

5.2 Gauss method

The Gauss method is a technique that assumes Keplerian orbits (propagation without perturbations) and considers the three position vectors to be in a single plane [18, 25]. This method was first developed to determine the orbit of interplanetary bodies, but it can also be applied to Earth's orbiting objects.

From three observations of the same object, the method consists of finding the roots of the following eight-order polynomial given by:

$$r_2^8 + ar_2^6 + br_2^3 + c = 0 \quad (15)$$

In Eq. 15, the parameters a, b and c are calculated from the observation times, line-of-sight vectors and observation site. By solving Eq. 15, eight roots are

found, but only one is a real and positive value. The remaining roots are imaginaries or negatives. Therefore, the single viable solution represents the magnitude of the position for the observation in the middle. After that, the slant range vector can be determined, and then the object position vector can be computed using Eq. 10.

5.3 Gooding method

The Gooding method is an iterative technique that requires three observations of the same object and initial guesses for the ranges of the first and third observations. It then iterates by slightly changing the initial guesses until it finds convergence [19, 25].

With the initial values of ranges, the position vectors of the first and the third observations can be computed using Eq. 10. Then, a Lambert solver is called to propagate the state until the time of the second observation. The Lambert solver is a method that computes the orbit of an object from two position vectors and the time of flight between these two positions [18]. After that, the position vector of the second observation is determined. Then, the line-of-sight vector from the estimated position is compared to the truth line-of-sight via a dot product. If the solution is near one, the method achieves the desired result.

The iterative part of this method involves slightly adjusting the range until the dot product between the estimated and true line-of-sight results approaches a value of one. This change is performed by varying the range's direction and magnitude. In other words, the method slightly modifies the range guess up and down to find the partial derivatives of this guess. Then, the partial derivatives are applied to a Newton-Raphson method to update the range for the next iteration.

The convergence of the Gooding method is directly connected to the initial guesses for the range. The chances of successfully reaching the convergence are higher if the initial guess is close to reality. So, the range calculated from the Gauss method was used as the initial guesses, as suggested by [26]. Moreover, the Lambert solver is also vital for the method's success. Therefore, the Lambert solver from GODOT was used.

5.4 Results

In total, 39 observations from all the detections were chosen for having a visible time interval larger than 20 seconds. Each object from these 39 has an ID number from 1 to 39. For example, the detected object number 1 has an orbit with a semimajor axis of 7000 km, an inclination of 66.67° and a RAAN of 59.17°, and it was visible for 20 seconds. In summary, each ID represents an object in a specific orbit.

The IOD was performed for each object a hundred times since each has a hundred angular data corrupted by the

star tracker uncertainty (see Subsection 5.1). After that, the Gauss and Gooding results were compared to the real value (the simulation output) to assess the accuracy of the IOD methods. Then, a difference between the real data's orbital elements, position and velocity magnitudes, and the IOD results was performed to check how far apart the method's outputs were. Finally, a mean and a standard deviation of the difference for each object were computed.

The comparison results for the semimajor axis, position and velocity are shown in Fig. 7, in Fig. 8 and in Fig. 9. In these figures, it is possible to see the mean difference error and the standard deviation for the Gauss and Gooding for each object ID. For the semimajor axis, Fig. 7, the error difference for almost all objects is below 200 km for both methods. This difference is sometimes less than 100 km. Also, both methods have similar behaviours, presenting results that are very close to each other. However, the Gooding method demonstrated a better performance in four cases.

Fig. 8 shows the position errors where almost all scenarios are below 250 km, in some cases below 100 km difference. The results of both methods are similar again, but Gauss performed better for two objects this time. The velocity errors concentrate below 0.2 km/s, as shown in Fig. 9, and Gooding performed slightly better for four scenarios.

In summary, Gauss and Gooding demonstrated promising results with errors of a few hundred kilometres for the semimajor axis and position and small errors for the velocity. The better results were obtained for objects with a semimajor axis of 7000 km and inclinations ranging from 49° to 85°. On the other hand, the worst findings were for more distance objects with semimajor axes of 7050 km and 7100 km.

Evaluating the remaining orbital elements, the methods

performed better for the inclination than the others. The average inclination errors were about 20°. It was less than 5° in four scenarios. The better results were for higher inclination orbits ranging from 85° to 102°, while the worst findings happened for orbits with 49° of inclination. Moreover, Gauss and Gooding failed to estimate eccentricity and RAAN with a few errors. Tab. 4 presents the results for some detected objects.

Tab. 4 presents the results for four different object orbits. Object ID 4 orbit has a semimajor axis of 7000 km, an inclination of 102.22° and a RAAN of 261.40°. Objects 17 and 19 have the same semimajor axis as object 4, but with inclinations of 66.67° and 75.55° and RAANs of 59.17° and 340.28°, respectively. Last, object 31 is in a higher orbit of 7050 km of semimajor axis, with an inclination of 93.33° and RAAN 182.50°. These orbits and the results in Tab. 4 indicate the performance of the methods discussed in the previous paragraphs. Gauss and Gooding can estimate the inclination more precisely for orbits with higher inclinations, but the semimajor axis, position and velocity have a greater uncertainty. On the other hand, the methods perform better for the semimajor axis, position and velocity in orbits with inclinations lower than 85°. Also, the object 31 results demonstrate that this performance decreases for higher semimajor axes.

The RAAN results are less bad for orbits with RAAN larger than 260°. A similar behaviour cannot be seen in the eccentricity estimation. The results for the eccentricity seem to be completely random and independent of the type of orbit. Moreover, Gauss and Gooding generally presented similar estimations, being able to compute the orbit with reasonable precision for the semimajor axis, position and velocity and estimate the inclination with fair accuracy for higher inclination orbits.

Table 4. Gauss and Gooding results for some detected objects

Object ID	$ \Delta\vec{r} $ (km)	$ \Delta\vec{v} $ (km/s)	Δa (km)	Δe	Δi (°)	$\Delta RAAN$ (°)
Gauss method						
4	128.27	0.08	115.54	0.008	4.62	36.78
17	72.95	0.04	71.61	0.001	31.00	240.97
19	74.44	0.04	81.44	0.0004	22.08	40.39
31	151.17	0.11	200.71	0.018	4.99	115.87
Gooding method						
4	128.27	0.08	118.60	0.008	4.62	36.78
17	72.95	0.04	71.54	0.001	31.00	200.86
19	74.44	0.04	81.80	0.0004	22.08	40.39
31	151.17	0.11	200.43	0.018	4.99	115.87

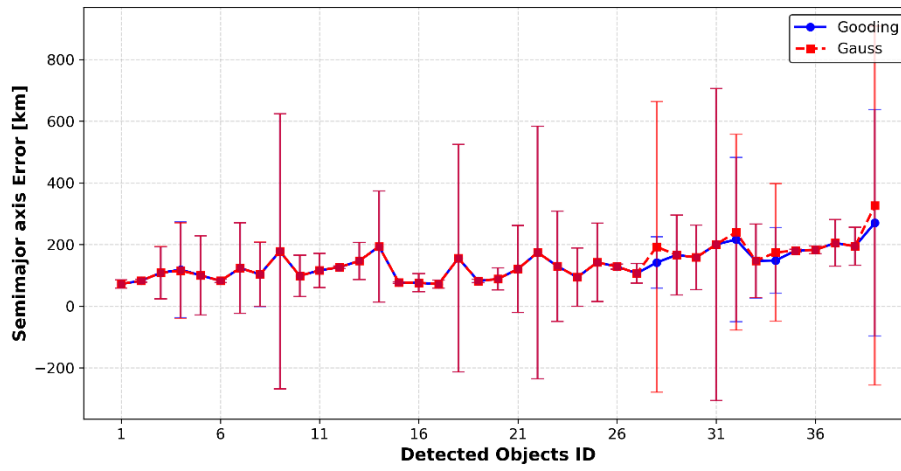


Figure 7. Semimajor axis errors.

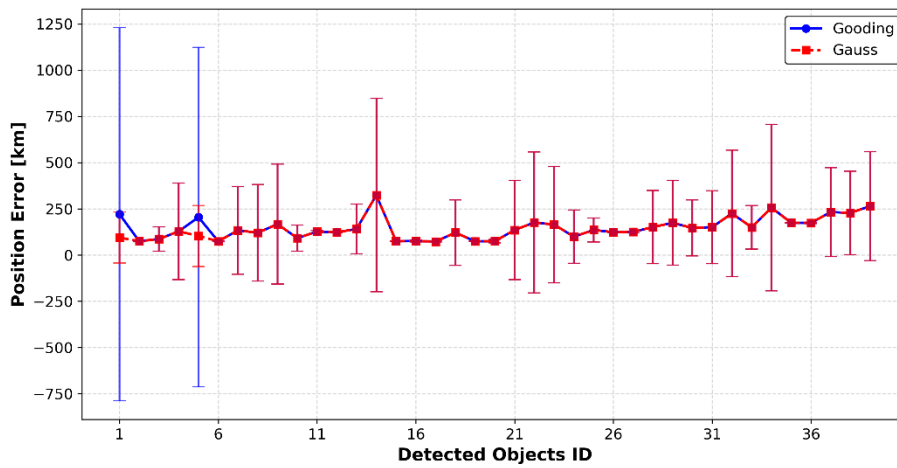


Figure 8. Position magnitude errors.

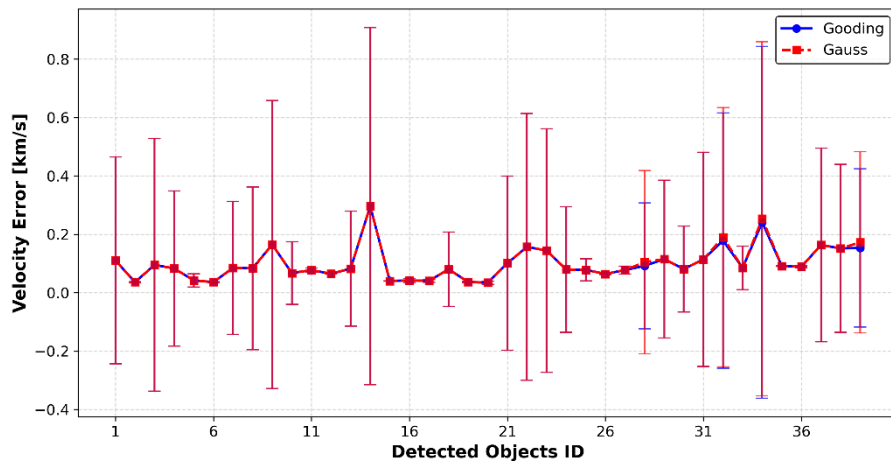


Figure 9. Velocity magnitude errors.

6 CONCLUSION

The continuous increase of space activities and space objects demands constant surveillance of space debris for the safety of space missions. This study explores the potential of using a star tracker to detect uncatalogued debris and contributes to a future catalogue of these objects.

The study started by identifying the most likely orbit to find sub-10 cm debris using MASTER. Then, the star tracker's performance in detecting these objects was evaluated. The results indicate that the proposed star tracker can detect uncatalogued debris at a maximum range of 400 km, depending on the object material. After that, a simulation using GODOT was conducted to verify whether the detection by the star tracker actually occurred. The simulations demonstrated that detections occur for objects in various orbits, indicating the capability of the star tracker to observe uncatalogued debris.

Finally, the orbits of the detected objects were computed using the Gauss and Gooding methods and compared with the simulation results to assess the accuracy of both techniques. The methods performed similarly, determining the semimajor axis, position and velocity with reasonable accuracy and the inclination with good precision for higher inclination orbits.

7 ACKNOWLEDGEMENT

Joel Filho acknowledges the support provided by the scholarship in the framework of the ESA Co-Sponsored Research Agreement, reference I-2022-04378, with the title Space Debris Algorithms on Satellite Constellation Pictures for Debris Characterisation and Orbit Determination through FCIências.ID, Universidade de Lisboa; Nuno Peixinho acknowledges funding by Fundação para a Ciência e a Tecnologia (FCT) through the research grants UIDB/04434/2020 (DOI: 10.54499/UIDB/04434/2020) and UIDP/04434/2020 (DOI: 10.54499/UIDP/04434/2020). The authors acknowledge the support provided by the Research project called Mobilising Agenda: New Space Portugal (Ref. C644936537-00000046, Notice ACC02/CO5-i01/2022), funded by the “Mobilising Agendas for Business Innovation” through the “Recovery and Resilience Programme (PRR)”; The authors acknowledge Fundação para a Ciência e a Tecnologia (FCT) for its financial support via the projects LAETA Base Funding (DOI: 10.54499/UIDB/50022/2020), LAETA Programmatic Funding (DOI: 10.54499/UIDP/50022/2020) and INESC TEC (DOI: 10.54499/UIDB/50014/2020).

8 REFERENCES

1. Bonnal, C., McKnight, D. S., & International Academy of Astronautics (IAA). (2017). *IAA*

- situation report on space debris 2016*. Paris.
2. NASA. (2020). *NASA Spacecraft Conjunction Assessment and Collision Avoidance Best Practices Handbook*.
3. NASA. (2021). *NASA'S EFFORTS TO MITIGATE THE RISKS POSED BY ORBITAL DEBRIS*. Retrieved from <https://oig.nasa.gov/hotline.html>.
4. ESA Space Debris Office. (2024). *ESA'S ANNUAL SPACE ENVIRONMENT REPORT, GEN-DB-LOG-00288-OPS-SD, Issue 8*. Darmstadt. Retrieved from https://www.esa.int/Space_Safety/Space_Debris/ESA_s_Space_Environment_Report_2024
5. Du, J., Chen, J., Li, B., & Sang, J. (2019). Tentative design of SBSS constellations for LEO debris catalog maintenance. *Acta Astronautica*, 155, 379–388. <https://doi.org/10.1016/j.actaastro.2018.06.054>
6. Spiller, D., Magionami, E., Schiattarella, V., Curti, F., Facchinetti, C., Ansalone, L., & Tuozi, A. (2020). On-orbit recognition of resident space objects by using star trackers. *Acta Astronautica*, 177, 478–496. <https://doi.org/10.1016/j.actaastro.2020.08.009>
7. Krutz, U., Jahn, H., Kührt, E., Mottola, S., & Spitz, P. (2011). Radiometric considerations for the detection of space debris with an optical sensor in LEO as a secondary goal of the AsteroidFinder mission. *Acta Astronautica*, 69(5–6), 297–306. <https://doi.org/10.1016/j.actaastro.2011.04.003>
8. Gruntman, M. (2014). Passive optical detection of submillimeter and millimeter size space debris in low Earth orbit. *Acta Astronautica*, 105(1), 156–170. <https://doi.org/10.1016/j.actaastro.2014.08.022>
9. Liu, M., Wang, H., Yi, H., Xue, Y., Wen, D., Wang, F., ... Pan, Y. (2022). Space Debris Detection and Positioning Technology Based on Multiple Star Trackers. *Applied Sciences (Switzerland)*, 12(7). <https://doi.org/10.3390/app12073593>
10. Shtofenmakher, A., & Balakrishnan, H. (2023). Effects of Phase Angle and Sensor Properties on On-Orbit Debris Detection Using Commercial Star Trackers. In *Proceedings of the International Astronautical Congress, IAC (Vol. 2023-October)*. International Astronautical Federation, IAF. <https://doi.org/10.1016/j.actaastro.2024.05.028>
11. Urru, A., Spanu, M., Congiu, E., Palmas, A., &

- Andronico, P. (2023). Performance index of a network of ground-based optical sensors for space objects observation and measurements. *Advances in Space Research*, 72(10), 4147–4156. <https://doi.org/10.1016/j.asr.2023.08.013>
12. Silha, J., Schildknecht, T., Hinze, A., Utzmann, J., Wagner, A., Willemsen, P., ... Flohrer, T. (2014). Capability of a space-based space surveillance system to detect and track objects in GEO, MEO and LEO orbits. *International Astronautical Federation*. Retrieved from <https://www.researchgate.net/publication/290349787>
 13. Chen, B., & Xiong, J. (2017). The Platform Design of Space-based Optical Observations of Space Debris. *Chinese Astronomy and Astrophysics*, 41(1), 109–124. <https://doi.org/10.1016/j.chinastron.2017.01.011>
 14. Du, J., Lei, X., & Sang, J. (2019). A space surveillance satellite for cataloging high-altitude small debris. *Acta Astronautica*, 157, 268–275. <https://doi.org/10.1016/j.actaastro.2019.01.003>
 15. Choi, E.-J., Cho, S., & Yoon, J.-C. (2019). Development of Space Surveillance Tracking and Orbit Determination Program. In *First Int'l. Orbital Conf. (2019)*.
 16. Montenbruck, O., & Gill, E. (2001). *Satellite Orbits: Models, Methods and Applications* (1st Edition.). Springer. Retrieved from <http://www.springende/phys/>
 17. Pastor, A., Sanjurjo-Rivo, M., & Escobar, D. (2021). Initial orbit determination methods for track-to-track association. *Advances in Space Research*, 68(7), 2677–2694. <https://doi.org/10.1016/j.asr.2021.06.042>
 18. Vallado, D. A. (2013). *Fundamentals of Astrodynamics and Applications* (Fourth Edition.). Hawthorne: Microcosm Press.
 19. Gooding, R. H. (1993). *A New Procedure for Orbit Determination Based on Three Lines of Sight (Angles Only)*. Farnborough.
 20. ESA. (2022). *Software User Manual-MASTER*. Retrieved from <https://sdup.esoc.esa.int>.
 21. Krag, H., Beltrami-Karlezi, P., Bendisch, J., Klinkrad, H., Rex, D., Rosebrock, J., & Schildknecht, T. (2000). PROOF — The extension of esa's MASTER Model to predict debris detections. *Acta Astronautica*, 47(2–9), 687–697. [https://doi.org/10.1016/S0094-5765\(00\)00106-5](https://doi.org/10.1016/S0094-5765(00)00106-5)
 22. Filho, J., Gordo, P., Peixinho, N., Melicio, R., & Gafeira, R. (2023). Payload Camera Breadboard for Space Surveillance—Part I: Breadboard Design and Implementation. *Applied Sciences*, 13(6), 3682. <https://doi.org/10.3390/app13063682>
 23. Flohrer, T. (2012). *Optical Survey Strategies and their Application to Space Surveillance*. Institut für Geodäsie und Photogrammetrie, Zurich.
 24. ESA/ESOC. (2021). GODOT. Retrieved June 5, 2024, from <https://godot.io.esa.int/docs/1.4.0/index.html>
 25. Miller, C. A., & Frueh, C. (2021). A COMPREHENSIVE COMPARISON AMONG CLASSICAL AND GOODING METHODS OF INITIAL ORBIT DETERMINATION IN OPTIMIZED ELECTRO-OPTICAL SENSOR NETWORKS. In *8th European Conference on Space Debris*. Darmstadt, Germany. Retrieved from <http://conference.sdo.esoc.esa.int>,
 26. Hwang, H., Park, S. Y., & Lee, E. (2019). Angles-only initial orbit determination of Low Earth Orbit (LEO) satellites using real observational data. *Journal of Astronomy and Space Sciences*, 36(3), 187–197. <https://doi.org/10.5140/JASS.2019.36.3.187>